



HAL
open science

Study of the photoluminescence enhancement observed in ZnO nanowire gratings optimally grown by hydrothermal method

Aubry Martin, Audrey Potdevin, François Réveret, Emmanuel Centeno, Rafik Smaali, Fatima Omeis, David Riassetto, Elena Kachan, Yves Jurlin, Geneviève Chadeyron, et al.

► To cite this version:

Aubry Martin, Audrey Potdevin, François Réveret, Emmanuel Centeno, Rafik Smaali, et al.. Study of the photoluminescence enhancement observed in ZnO nanowire gratings optimally grown by hydrothermal method. 2023. hal-03976648v1

HAL Id: hal-03976648

<https://hal.science/hal-03976648v1>

Preprint submitted on 7 Feb 2023 (v1), last revised 9 Nov 2023 (v2)

HAL is a multi-disciplinary open access archive for the deposit and dissemination of scientific research documents, whether they are published or not. The documents may come from teaching and research institutions in France or abroad, or from public or private research centers.

L'archive ouverte pluridisciplinaire **HAL**, est destinée au dépôt et à la diffusion de documents scientifiques de niveau recherche, publiés ou non, émanant des établissements d'enseignement et de recherche français ou étrangers, des laboratoires publics ou privés.

Study of the photoluminescence enhancement observed in ZnO nanowire gratings optimally grown by hydrothermal method

Aubry Martin^{1,2}, Audrey Potdevin^{2,*}, François Réveret², Emmanuel Centeno³, Rafik Smaali³, Fatima Omeis^{3,4}, David Riassetto¹, Elena Kachan⁴, Yves Jourlin⁴, Geneviève Chadeyron² and Michel Langlet^{1,‡}

¹ Université Grenoble Alpes, CNRS, Grenoble INP, LMGP, 38000 Grenoble, France

[‡] e-mail : michel.langlet@imgp.grenoble-inp.fr

² Université Clermont Auvergne, CNRS, Clermont Auvergne INP, ICCF, F-63000 Clermont–Ferrand, France. *e-mail: audrey.potdevin@sigma-clermont.fr

³ Université Clermont Auvergne, CNRS, Clermont Auvergne INP, Institut Pascal, F-63000 Clermont–Ferrand, France.

⁴ Laboratoire Hubert Curien, Université de Lyon, UMR CNRS 5516, 42000 Saint-Etienne, France

Abstract

We report for the first time the elaboration of an original ZnO nanowire (NW) architecture entirely based on a soft chemistry approach and its thorough assessment through optical measurements and electromagnetic simulations. This architecture relies on the photo-imprinting of a sol-gel ZnO-based photosensitive seed layer combined with the subsequent localized hydrothermal growth of ZnO NWs. We firstly show how optimization of the elaboration protocol leads to uniform and reproducible linear and periodic gratings of ZnO NWs with a width / pitch of 2 μm / 4 μm . For reference, full-covered samples (NWs coating) have also been elaborated from a non-imprinted seed layer. It has been evidenced through morphological study that NW gratings present a peculiar profile similar to a hedgehog. Standard and angle-resolved photoluminescence measurements performed on both kinds of samples are then presented. These optical characterizations demonstrate that ZnO NW visible emission is strongly modified by the presence of NW gratings and that its red part is directionally extracted and increased by a factor up to 2. We present finally electromagnetic simulations performed for both samples which highlight the role of the gratings acting as coupled microcavities that boost the ZnO emission thanks to light localization and diffractive mechanisms. It enables the extraction of the resonant photons towards some specific angles and at given wavelengths.

Keywords: ZnO nanowires; resonant gratings; photoluminescence enhancement; electromagnetic simulations

Introduction

Nanowires (NWs) are advanced structures developed in recent years for multiple applications, due to their high aspect ratio (length to width ratio) inducing specific properties which differ from bulk materials^[1]. This is due to the fact that electrons are laterally quantum confined in the NWs and thus occupy different energy levels^[2]. For example, bulk silicon presents an indirect band-gap, while silicon nanowires have a direct band-gap, making them good candidates for optoelectronic applications. Their use has thus grown lately, fostered by the need for ever-miniaturized devices, for example in metal oxide semiconductor field-effect transistors^[3] in the case of silicon NWs. Another application of the latter is their exploitation to improve solar devices, as described by Yu *et al.*^[4], where NWs are used

preferably to bulk silicon as they reduce bulk recombination. Besides, thanks to their specific geometry, NWs present less internal defects than bulk materials and a high crystallinity. In contrast, their intrinsically high specific surface area induces more surface defects, which can be interesting for some applications. It has been shown for example that surface defects of ZnO NWs emit in the visible range and in particular in the orange-red wavelengths when excited by UV (λ_{exc} lying between 325 and 395 nm)^[5,6]. NW arrays can also increase the light extraction efficiency (LEE)^[8,9] since 1/they bring more roughness to a surface when deposited on it which induces light scattering, and 2/ they can create a refractive index gradient which favors photons extraction. This property is of great interest to improve the efficiency of light-emitting diodes (LEDs) devices as H. Jeong *et al.*^[10] or L. Huang *et al.*^[11] highlighted using ZnO nanowires.

Along with NW arrays, other strategies have been developed to improve and to control the light emission of optoelectronic devices. The diffractive properties of periodic structures such as gratings or photonic crystals have been used to both enhance the LEE but also to select the light emission direction^[12–15]. Structuring the material on the scale of hundreds of nanometers (corresponding to the emission wavelength in this medium) allows modes trapped in a guiding layer to be efficiently extracted. ZnO NW arrays patterned like a 2D photonic crystal have for example demonstrated a 34% increase in emission intensity of GaN based blue LEDs^[16] and have enabled significant enhancement of the luminescence and lasing behavior^[17]. Beside this dielectric approach, plasmonic components using metallic nanoparticles^[18] or subwavelength periodic structures have also been investigated^[19,20]. Using this kind of approach, radiation properties of localized surface plasmon can also help for the light extraction.

Among various possible materials to which the aforementioned structuring strategies could be applied, we have decided to focus our attention on ZnO and derived NW gratings. Indeed, ZnO is an affordable and ecofriendly material with many interesting characteristics such as a wide-band gap energy of 3.37 eV at room temperature and an exciton binding energy of 60 meV. It is an n-type semiconductor and ZnO NWs find applications in various domains, such as in LED devices as light extraction enhancer as mentioned before^[10], photodetectors^[21], and to create hydrophobic^[22] or super-hydrophobic and self-cleaning surfaces^[23]. Recently, ZnO NW gratings have been developed by different processes. The two most common ones are chemical vapor deposition (CVD) and hydrothermal growth. For example, Cheng *et al.*^[24] obtained various ZnO nanowire structures, including gratings, by CVD from a patterned photoresist. This approach, although efficient, stays quite expensive and requires devoted equipment. On the contrary, the hydrothermal method is based on growing NWs from a seed layer in a bath containing zinc precursors. This soft chemistry method is less costly and similarly allows to create ZnO NW structures. The grating structures themselves can be obtained by two main methods. One consists in using a template, that can be a pre-patterned gold substrate on which ZnO NWs grow, such as in Obreja *et al.*'s work^[25], or an organic sacrificial template^[26,27] which is removed afterwards. The other method is based on the direct engraving of the seed layer, by employing a photosensitive zinc-based resist. Park *et al.*^[28] used this way to obtain ZnO NW gratings by ultraviolet assisted nanoimprint lithography (NIL). Residual resist between the patterns had then to be removed using a Cl_2 plasma, adding a complex step to the process. Furthermore, derived nanowires had a weak aspect ratio below 5 and/or they grew in the form of disordered flower-like patterns, without any preferential direction.

In this article, we present for the first time an original method based on the UV-engraving of a sol-gel ZnO-based photosensitive seed layer combined with hydrothermal growth and leading to dense and rather vertically aligned ZnO NW gratings. The pattern combines both micro- and nano-structuration by using a periodic set of micrometric microcavities made of ZnO NWs. This original

structure should benefit both from scattering effect brought by the topographical changes due to the NWs and from the expected diffraction effects due to the presence of the grating. The study of these architectures will be presented in several stages. First, the synthetic protocol to obtain ZnO NW gratings will be detailed, as well as optimization steps of this process. Then, the morphological study of the obtained structures, led by Scanning Electron Microscopy (SEM) and Atomic Force Microscopy (AFM), will be presented. Standard and angle-resolved photoluminescence (ARPL) results will be shown and discussed. In particular, optical features of ZnO NW gratings will be compared to fully covered ZnO NW samples ("NW coatings"). Electromagnetic simulations were performed for both kinds of samples in order to better understand the mechanisms involved in their optical behavior and in particular within the multi-scale architectures.

Experimental section

i/ Elaboration of ZnO nanowires

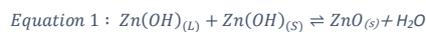
The elaboration of ZnO nanowire gratings was performed through hydrothermal growth from a previously deposited crystalline ZnO seed-layer. In the following section, the elaboration of the seed-layer will first be detailed, and then the growth step will be described. The seed-layer is originated from a sol-gel based procedure that was previously established in our group.^[29] The sol is constituted of 0.36M of zinc acetate dehydrate (ZAD) and monoethanolamine (MEA) in equimolar quantities and diluted in 1-butanol. The ZAD is used as zinc source whereas MEA serves to control the basicity of the solution. The sol is then aged by stirring at 90°C for 3 hours.

In the case of gratings, this process has been adapted from the work of Kawahara *et al.*^[30,31] in order to obtain a positive photoresist, *i.e.* that directly reproduces the pattern of a chromium mask. Such a resist is the key to the selective growth of ZnO nanowire gratings that will be the subject of the discussions below. The adaptation consisted in the addition of benzoylacetone (BzAc, 0.34M) to the sol before the aging process. Benzoylacetone forms chelation rings with zinc, which leads to a stable Zn-BzAc resist when immersed in acidic solution. In contrast, the chelate is chemically destabilized by photo-hydrolysis when exposed to UV irradiation, and the resist can be removed from the substrate by dilution in acidic medium. It allows thus its local elimination after selective UV exposition through a chromium mask.

The so-obtained Zn-BzAc photosensitive sol was deposited by spin-coating a 300 μ L droplet for 10s at 3000 rpm on 3x3 cm² (100) silicon wafers and 2.5x2.5 cm² quartz substrates. It was then dried and partially stabilized at 110°C for 30min in an oven before being introduced in an UV-insulation device (UV-KUB from KLOE Company) operated at a 365 nm wavelength. For the selective insulation, we used a quartz mask with chromed linear gratings of 2 μ m / 4 μ m width / pitch as illustrated in Figure S1, and the insulation was performed for 40 minutes. As the mask was put in contact with the resist over insulation, it was necessary to thoroughly clean it with acetone before each insulation to remove any trace of the resist that would affect the next insulation and the quality of resulting gratings.

After insulation and a short post-baking at 110°C for 8 minutes, the sample was dipped in a development bath of nitric acid at pH=3 in order to etch the insulated parts of the photoresist and to reveal the grating patterns. To reduce experimental variability, *i.e.* improve the grating uniformity and reproducibility, etching was performed in a crystallizing dish by dipping the sample horizontally into the acidic solution for 30 s, before washing with deionized water and subsequent drying. The sample was then annealed for 1 hour at 540°C to form a crystalline ZnO seed-layer structured in the form of linear gratings separated by denuded stripes of the substrate.

For the NW growth step, we also used a protocol developed in our group^[29]. A growth bath constituted of an equimolar aqueous solution of hexamine (HMTA) and zinc nitrate (ZN) was prepared and heated at 90°C. The concentration of both chemicals was initially fixed at 0.025M, and further optimization will be described in the next part of the text. The seed-layer coated substrate was cleaned with an O₂ plasma (12V, 3min) before being attached to a home-made Teflon® sample holder, facing down and inclined at 45° to limit the deposition of pollutants arising from homogeneous growth in the liquid medium. Then, it was dipped for 30 min in the growth bath stirred at 500 rpm. This operation led to the localized hydrothermal growth of the nanowires on the structured seed-layer according to Equation 1, where Zn(OH)_(l) represents the reactive species in solution and Zn(OH)_(s) the reactive species at the surface of the substrate.



The sample was then washed with deionized water and subsequently dried with a nitrogen flow. It resulted in the elaboration of NW gratings according to an original procedure that, as far as we know, has never been described before in the literature.

ii/ Characterization techniques

Morphological features of ZnO NWs were mainly studied by SEM and AFM. The complementarity of both methods used to assess the NW gratings will be analyzed in the next part of the text. The SEM employed was a ZEISS Gemini300 operated with a voltage of 3 kV and using an in-lens detector at a working distance of 6 mm. For the AFM, we used a JPK Nanowizard 4 with OTESPA probes. The emission properties of the samples were measured at room temperature using standard and ARPL set-up. The second harmonic (375 nm) of a Ti:sapphire laser was used to illuminate the sample from the backside of quartz substrates supporting ZnO nanowires. The PL signal was detected by an optical fiber mounted on a goniometer to collect emission from 0°, *i.e.* perpendicularly to the substrate, to 90° with an angular resolution of 0.6°. The signal was then focused on the slit of a 32 cm focal monochromator and detected by a CCD camera (Figure S2 presents a scheme of the set-up).

iii/ Electromagnetic simulations

The dispersive properties of the ZnO NW gratings were calculated with a finite element method implemented in Comsol Multiphysics. We simulated a unique cell with boundary conditions in the periodic directions of the grating and perfect matched layers (PML) in the perpendicular directions. The eigenmodes and complex eigenfrequencies were computed for the Block wavenumber lying in the first Brillouin zone. The quality factor and resonant wavelengths were derived from these eigenfrequencies.

Results and discussion

i/ Optimization of the elaboration process

The localized growth of uniform and reproducible NWs required an accurate control of numerous experimental parameters. For instance, the mask acetone cleaning and O₂ plasma cleaning of the insulated seed layer appeared as essential steps and were preliminarily optimized. Preliminary studies led as well to an optimization of the insulated photoresist development pH and procedure. In the next part, we focus on the optimization of two key parameters that strongly conditioned the robustness of our protocol, enabling to obtain uniform, reproducible and tunable ZnO NW gratings. These optimization steps were conducted on (100) silicon wafers.

Using the protocol detailed in the experimental section, individual or aggregated ZnO microrods were frequently observed to pollute the NW gratings, as illustrated in the SEM image of Figure 1. Those ZnO rods are characteristic of a homogeneous growth mechanism where particles directly form in suspension in the growth bath according to a mechanism similar to that depicted in Equation 1 but where $\text{Zn(OH)}_{(L)}$ react with themselves instead of reacting with $\text{Zn(OH)}_{(S)}$. This phenomenon competes with the expected heterogeneous growth mechanism, where the ZnO NWs form on the seed layer. Besides, homogeneous growth partially consumes the zinc precursor in the growth bath, which reduces the precursor amount available for reaction with the seed layer, and thus limits the growth of NWs. Accordingly, very short NWs were observed to grow with a length typically ranging between 200 and 350 nm and a resulting mean grating height of 250 nm, as shown by the AFM profile of Figure 1.

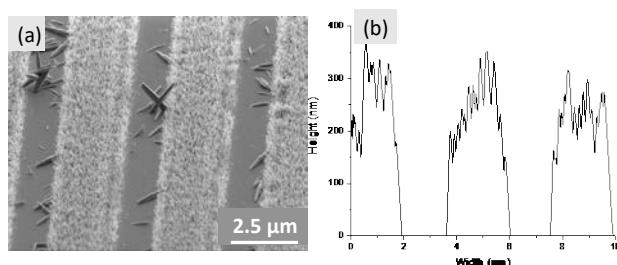


Figure 1: SEM Image showing the coexistence of linear NW gratings and big ZnO rods (a) and AFM profile of resulting gratings (b).

In Figure 1(b), the noisy AFM profile actually depicts NWs constituting the gratings, whereas the curved grating top depicted by AFM will be explained later. In order to limit the effects of the homogeneous growth, we proceeded to a reduction in the concentration of the zinc precursor in solution from 0.025M to 0.0125M, and we reduced equally the HMTA amount in solution to respect the initial equimolar proportions between ZN and HMTA. The 0.0125M ZN concentration appeared as an ideal trade-off intended to i/ reduce the interaction probability between precursor molecules in solution and thus minimize the homogeneous growth mechanism, and ii/ keep enough zinc precursor in solution available for the heterogeneous growth mechanism. This first optimization proved to be efficient since, as depicted by the two examples illustrated in Figure 2, it allowed to get rid of most of the ZnO microrods that polluted the surface and to obtain NW gratings with a consistently enhanced height of 500 to 600 nm. This enhanced height proves that, despite a weaker concentration of ZN in the growth bath, the elimination of the homogeneous growth mechanism leads to an increased amount of Zn precursor available for the NW growth at the seed layer surface.

Another key step of our protocol is the insulation of the photoresist. This step, as detailed in the experimental section, aims at monitoring the chemical reactivity of specific areas of the Zn-BzAc resist so that they can be then selectively etched to obtain grating patterns. In consequence, the insulating power is an important parameter whose influence has been studied and optimized. In preliminary experiments, we observed that, for an insufficient power as well as an excessive one, the resulting NW growth proceeded all over the substrate without considering the insulated gratings pattern (Figure S3). We have no clear explanation for both trends, but we make some assumptions. On the one hand, it is possible that a weaker insulating power may not be sufficient to fully activate photo-hydrolysis of the resist, which would result in an ineffective selective etching. On the other hand, we suppose that an excessive power can induce a certain warming-up of the resist that would be

sufficient to chemically stabilize it, again resulting in an ineffective etching in the presently adopted experimental conditions. Accordingly, the best insulation conditions stemmed from a moderate power around 25 mW/cm². Figure 2 illustrates NW gratings obtained after insulation with a power of 23.5 and 25 mW/cm². For both powers, the figure illustrates microrod-free and uniformly linear gratings separated by totally denuded stripes of the substrate. However, it can also be seen that even a small insulating power difference (6% in the examples illustrated in Figure 2) leads to significant changes in the features of ZnO NW gratings.

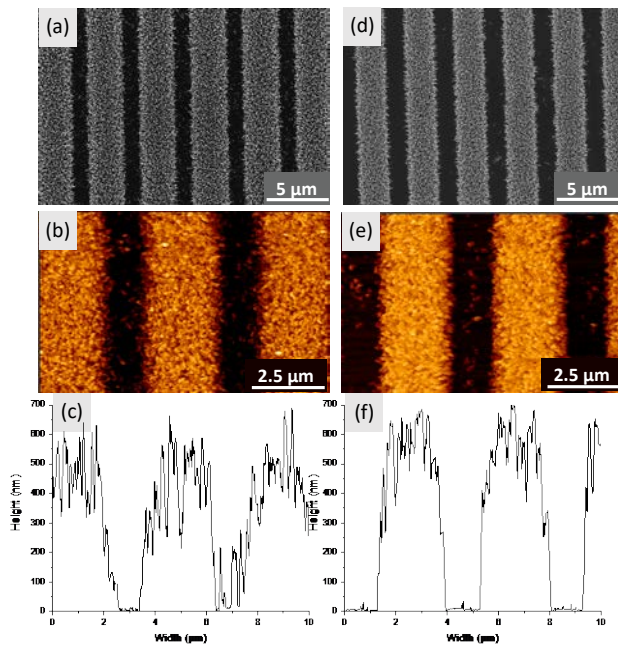


Figure 2: From top to bottom, SEM top view and AFM top view and profiles of ZnO NW gratings on silicon obtained after insulation at a power of 23.5 mW/cm² (a to c) and 25 mW/cm² (d to f).

On the one hand, the AFM profiles of Figure 2 indicate a slightly weaker mean grating height for a power of 23.5 mW/cm² (around 500 nm – Figure 2(c)) compared to a 25 mW/cm² one (around 600 nm – Figure 2(f)). On the other hand, AFM and SEM top view images show that the weaker power leads to significantly wider gratings (around 2.8 μm width) compared to those obtained after an insulation at 25 mW/cm² (around 2.3 μm width). Thus, the higher power apparently results in a grating width much closer to but still greater than the expected one (2 μm according to the mask patterns illustrated in Figure S1). However, a closer inspection of the grating profile enables to draw further conclusions. Figure 3 illustrates SEM cross section images of gratings obtained after insulation at a 25 mW/cm² power. These images highlight the uniformity of NW diameters with a value around 40 nm. It can then be observed that NWs do not grow perfectly vertically, and their inclination tends to increase on the grating edges, leading thus to a kind of reentrant grating profile, similar to a hedgehog. This NW inclination explains the curved top of the gratings, as illustrated by AFM profiles (Figure 1(b) and Figure 2(c) & (f)). In particular, according to such reentrant profiles, Figure 3 shows that, for an insulating power of 25 mW/cm², the grating width closely matches the expected value of 2 μm at the NWs-seed layer interface, and this width tends to progressively increase near the top of the gratings.

This observation has several practical consequences. It firstly means that AFM and SEM top view images account for the top of the gratings and necessarily depict a larger width than the expected one. It also means that, since the AFM tip cannot reliably probe structures with reentrant profiles, AFM profiles shown in Figure 1(b) and Figure 2(c) & (f) do not rigorously account for the real grating profile. These features highlight therefore that, in the frame of this work, AFM and SEM characterizations provide useful complementary information. The former enables to precisely quantify the NW lengths and grating heights while the latter enables to reliably probe the exact grating profile. According to all these considerations, the insulating power was definitely set to 25 mW/cm² in following studies.

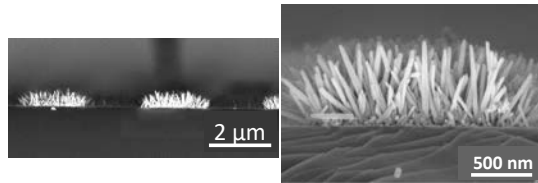


Figure 3: SEM cross section images of ZnO NW gratings on silicon obtained after insulation at a 25 mW/cm² power.

To assess the robustness of our optimized protocol, we studied the uniformity and reproducibility of NW grating on the surface of 3x3 cm² Si wafers. The photograph of Figure 4a depicts uniform diffraction features which provide first evidence that NW gratings have been elaborated in a homogeneous way on the whole substrate surface. This homogeneity is clearly illustrated by the SEM image at low magnification of Figure 4b. The high magnification SEM top view of Figure 4c shows that the gratings are constituted of uniformly distributed NWs whose density at the grating top has been approximately determined to be 190 NWs/μm². Figure 5 illustrates a SEM top view mapping of gratings elaborated on the entire surface of a 3x3 cm² Si wafer. As previously explained, such SEM data do not directly account for the real grating width, but they provide a reliable assessment of the grating uniformity. Accordingly, the mapping of Figure 5 shows reproducible gratings all over the substrate surface with a width (near the grating top) of 2.1 +/- 0.2 μm. These features enable us to definitively conclude to the robustness of our protocol.

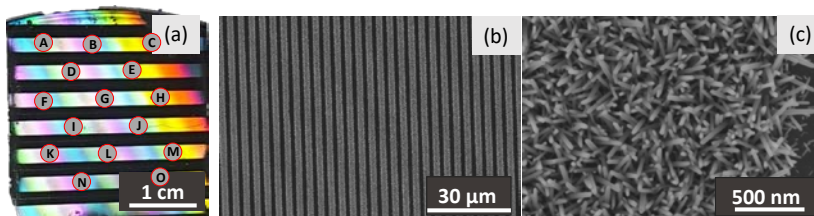


Figure 4: Large scale photograph (a) and SEM images at low (b) and high (c) magnifications of NW gratings elaborated on 3x3 cm² Si wafers after insulation at a 25 mW/cm² power. In the photo, the 15 areas noted A to O indicate where SEM images of Figure 5 have been considered.

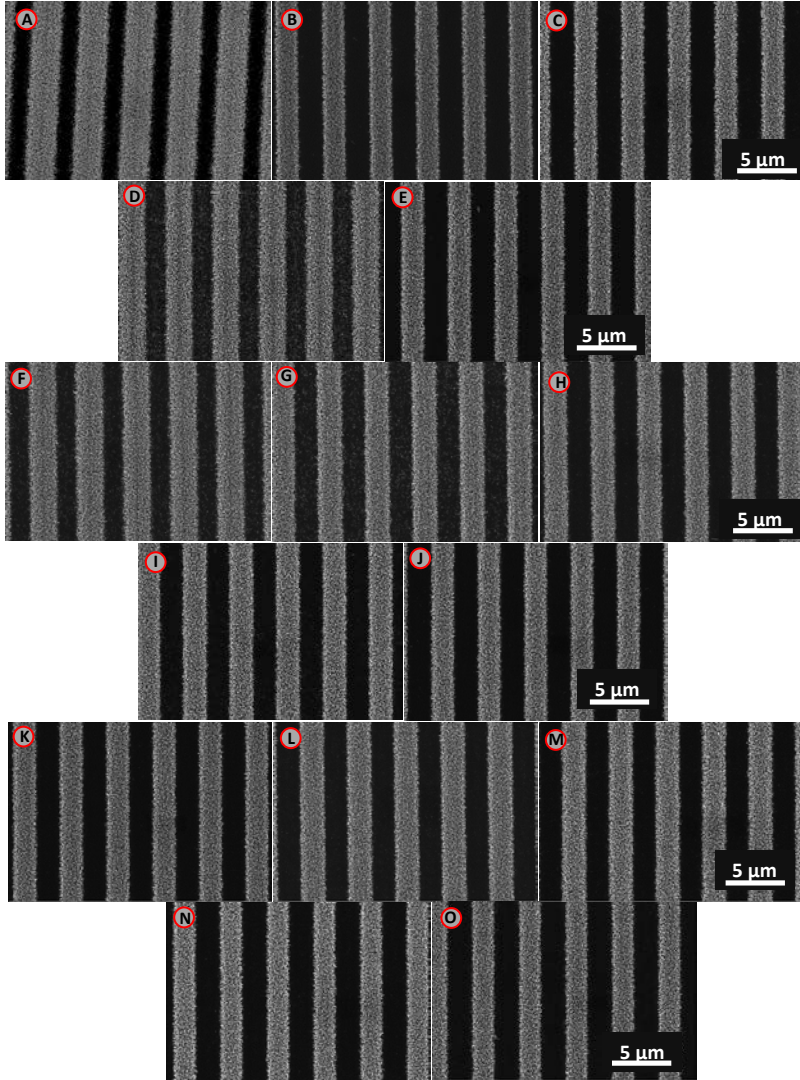


Figure 5: SEM top view mapping of ZnO NW gratings on a 3x3 cm² Si wafer obtained after insulation at a 25 mW/cm² power. The localization of areas A to O is depicted in Figure 4a.

This protocol, thoroughly optimized on Si wafers, has then been successfully extrapolated to quartz and glass substrates, which present numerous interests for optical applications. In the following, we focus on quartz substrates that will be then exploited in the frame of optical characterizations. The main grating features on 2.5x2.5 cm² quartz substrates are summarized in Figure 6. Globally speaking, this figure illustrates identical features as those previously depicted on silicon substrates, *i.e.* similar homogeneous diffraction effects at the macroscopic scale, uniformly linear gratings with a width and mean height near to those obtained on silicon, as well as a comparable NW diameter around 45 nm. Only some minor differences have been identified through the analysis of SEM data, namely a weaker

NW density of about $160 \text{ NWs}/\mu\text{m}^2$. Such minor differences, which may arise from the chemical nature and/or topology of the substrate, have not yet been clearly explained.

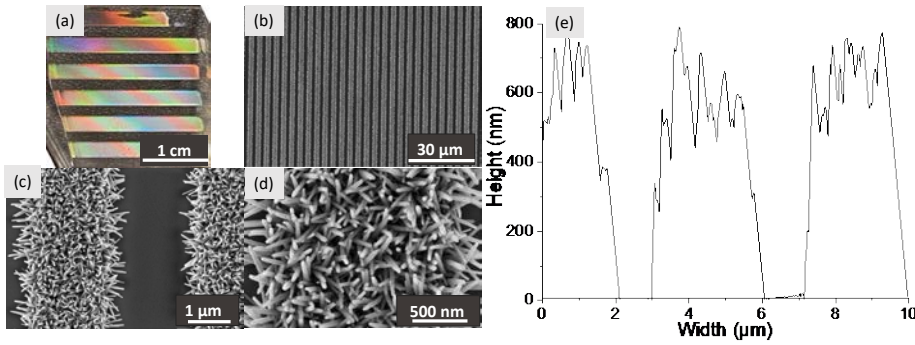


Figure 6: ZnO NW gratings on $2.5 \times 2.5 \text{ cm}^2$ quartz substrate illustrated by macroscopic photography (a), low (b) to high magnification (d) SEM images, and AFM profile (e).

ii/ Optical characterizations

To thoroughly study the optical properties of the elaborated ZnO NW structures, ARPL spectra were recorded at room-temperature (300 K) for both ZnO NW coatings (full coverage) and ZnO NW gratings. These emission spectra were recorded with a backside excitation source emitting at 375 nm and the angle of the detector varied between 0° (source and detector were aligned on each side of the sample) to 90° (detector on the edge of the sample, perpendicular to the source – see Figure S2). Characteristic emission profiles of these samples recorded at 0° are presented in Figure 7. Both spectra exhibit a large emission band between 400 and 800 nm, centered around 600 nm, in the orange-red spectral range. This large emission band has already been reported in the literature and is explained by radiative recombination processes caused by defects (oxygen and zinc vacancies) on the surface of the nanowires^[5,6,32]. It should be noted that several spurious emission signals attributed to the experimental set-up (second harmonic of the excitation source at 750 nm and other signals linked to the set-up) are also observed between 750 and 900 nm. Another set-up has also been used to record emission spectra on the same samples, exciting them from the front at a fixed angle of 45° . The corresponding spectra are gathered in Figure S4 (with a description of the set-up): they only present a large emission band lying from 400 to 800 nm, without the afore observed spurious signals, confirming these latter are due to the ARPL set-up.

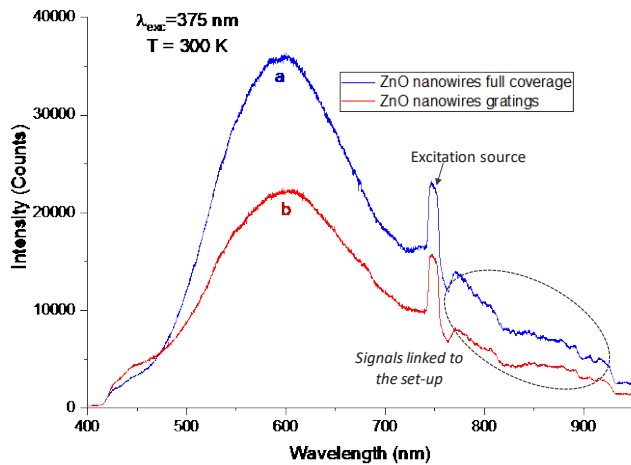


Figure 7: Room-temperature emission spectra recorded using a backside excitation at 375 nm on (a) a ZnO NW coating (full coverage) and (b) a ZnO NW grating grown on quartz.

The evolution of emission intensity as a function of wavelength and detection angle has been plotted for both kinds of samples. Resulting luminescence maps are gathered in. A quick glance shows a very significant influence of the grating (b) as its emission intensity is strongly enhanced in a specific angular range between 60 and 70° whereas the full covered sample (a) is characterized by a strong emission intensity that changes little when the detection angle is lying between 0 and 50°.

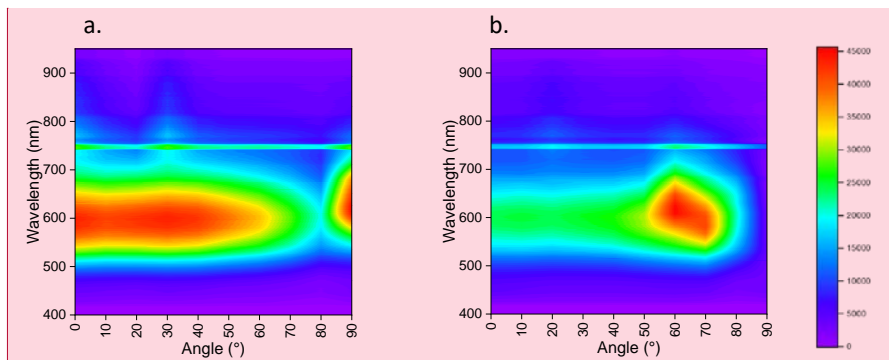


Figure 8: Room temperature ARPL map showing the evolution of the emission intensity with the wavelength and detection angle for (a) the ZnO coating and (b) the ZnO grating under 375 nm excitation

To facilitate the interpretation of these results, we have plotted the photoluminescence intensity at 600 nm versus the emission angle (Figure 8 Figure). The main trends identified on the Figure 7 Figure are confirmed. Accordingly, the emission of the ZnO NWs coating as a function of the observation angle ((Figure 8a Figure a) shows an almost constant emission intensity around 600 nm between 0° and 50°. The intensity decreases then with further increase of the emission angle, losing about 50% of its value at 80°. Beyond 80°, we observe a noticeable increase in the emission intensity that reaches values

Commenté [g1]: En ordonnée je propose d'ajouter "Emission wavelength "

comparable to the initial emission (below 50°) for angles greater than 85°. The strong intensity measured between 85 and 90° is explained by the extraction of guided modes trapped into the ZnO NW coating (and perhaps into the quartz substrate).

In contrast, the grating structuration significantly modifies the emission. As highlighted by the Figure 8b Figure b, while the emission is rather constant between 0° and 40°, it is approximately 40% lower than for a full covered sample. This result is partly justified by the quantity of emitting centers being twice as low for the gratings. As already illustrated in Figure 78, the main changes brought by the grating structuration are observed at greater angles where the emission intensity is observed to strongly increase and to reach a value about twice greater than the initial one for angles between 60° and 70°. Beyond 70°, we observe a continuous decrease in intensity leading to a minimum value, almost 7 times weaker than the value at 0°, for an angle of 90°. These results clearly demonstrate that the grating structure allows a light extraction enhancement of the guided modes leading to an emission intensity increase for emission angles around 60-70°. Over this angular range, there is therefore a strong exaltation of the luminescence emission of the ZnO NW gratings, largely exceeding the maximum emission intensity of the full covered sample while there are only half as many emitting centers.

Commenté [g2]: Je propose de supprimer ceci
 Commenté [AP3]: on laisse et on ajoute la publie de G. Dantelle

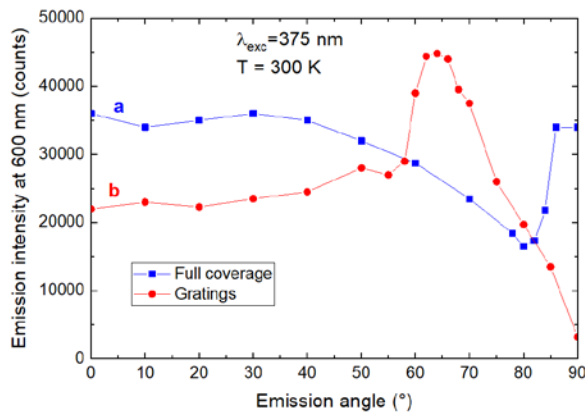


Figure 9: Angle dependent emission intensity ($\lambda_{em}=600$ nm, backside excitation at 375nm and 300K) for (a) a ZnO NW coating and (b) a ZnO NW grating.

To study more precisely the emission behavior induced by the presence of the gratings, an enhancement factor has been determined by dividing the emission spectrum data obtained at a fixed angle by those of the spectrum recorded at 0°. This enhancement factor is plotted in as a function of wavelength for angles between 50 and 70°. For an angle of 50° (in black), the spectrum presents a profile similar to the classical emission spectrum with a large maximum intensity centered around 600 nm, which reflects an overall increase in emission intensity over the entire wavelength range without any change in the spectrum profile.

This is not the case for greater emission angles where the enhancement factor exhibits a significant asymmetry. This later is particularly marked at 58° (in purple) and 60° (in dark blue) where the light extraction due to the grating is favored in the red region, and the emission enhancement factor is maximal around 700 nm at 58°. Then, when increasing the emission angle, the asymmetry of the enhancement factor progressively disappears and the maximum gain shifts towards the lower

wavelengths, from 700 nm (for 58°) to about 575 nm (for 70°). The most homogeneous contribution in terms of wavelength range is obtained for an angle of 62° (in bright blue) with a significant gain lying in the 500-750 nm range.

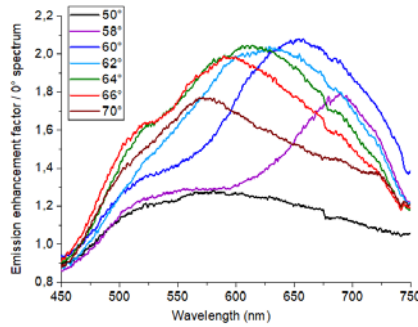


Figure 10: Emission enhancement factor compared to the spectrum at 0° versus emission wavelength for angles between 50° and 70°, measured on a sample containing ZnO NW gratings.

This study shows therefore that, for some angles, the grating structure makes it possible to exalt specific wavelengths that do not necessarily correspond to the emission maximum intrinsically due to the NWs. This complex behavior, together with the strong intensity enhancement of photoluminescence observed in **Erreur ! Source du renvoi introuvable.** 6 and 7, suggest the presence of a resonant electromagnetic mode within the grating structure.

Commenté [g4]: ??

Commenté [g5]: Ce doit être 7 et 8

The experimental dispersion curve is obtained by monitoring the angular position of PL emission peaks for a set of wavelengths between 590 nm and 700 nm. To draw it, the wavelength corresponding to the intensity peak is plotted as a function of the wavenumber $k_x = k_0 \sin \theta$ expressed in $\frac{2\pi}{D}$, where $k_0 = \frac{2\pi}{\lambda}$ and D is the grating period (Figure 10 Figure). The error bars correspond to the measurement uncertainty of 1° for the emission angle θ .

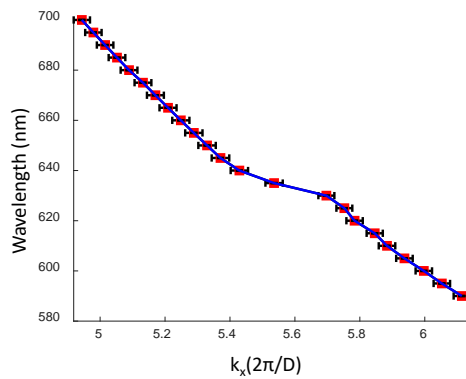


Figure 11: Experimental dispersion relation obtained from angle-resolved PL data.

The dispersion curve flattens between 5.4(2π/D) and 5.7(2π/D) suggesting an abnormal dispersion around 630 nm.

iii/ Simulations

To understand the origin of the enhancement of PL produced by the grating, we considered a bidimensional problem depicted in [Figure 11](#). Since the set of NWs present a complex random spatial distribution, we replaced the ZnO NWs by a homogeneous layer of refractive index n_h . This refractive index is estimated using a Maxwell-Garnet homogenization formula^[33] :

$$n_h = [n_{ZnO}f + n_0(1 - f)]^{0.5} \quad (2)$$

where n_{ZnO} and n_0 are the refractive indices of ZnO and air, respectively, and f is the filling factor of ZnO. In two dimensions, f is about 0.57 for a NW density around 200 NW/ μm^2 and for a NW diameter of ~ 40 nm. Considering that the optical index of ZnO is close to 2, n_h is approximately equal to 1.65, larger than the quartz substrate (1.45). This model enables us to determine the dispersion relation of the modes that propagate within the ZnO coating layer whose thickness has been set to 600 nm. We found two modes for both TE and TM polarization cases, (see SI, [Figure SI.X](#)). The fundamental modes present similar effective indices which are higher than those of the second antisymmetric-like modes (see SI, [Figure SI.X](#)). Here, we focus on the fundamental one whose wavenumbers is denoted $\beta = k_0 n_{eff}$. Its effective index n_{eff} is almost nondispersive and close to 1.6. This result confirms that the ZnO NW coatings support guided modes responsible for the emission recorded around 90° (see [Figure 7a](#) [Figure a](#) or [Figure 8a](#) [Figure a](#)).

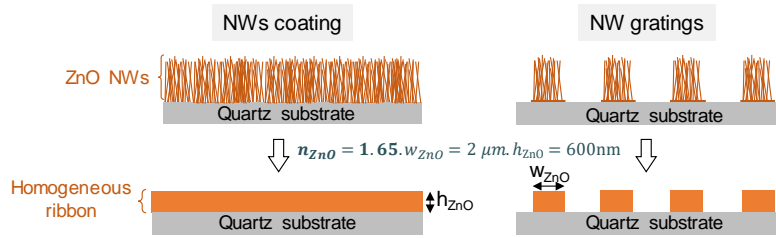


Figure 12: Schematic representation of the modelling of ZnO NW coating and grating by solid blocks. The main parameters used are noted in the center of the figure.

The grating structure can therefore be considered as a periodic set of truncated waveguides. Each finite length waveguide forms a cavity of width W , which has its own resonances built by the guided modes that interfere constructively. These resonances can be caught by a simple Fabry-Perot model^[34] whose reflection coefficient is given by:

$$r = \frac{\rho(1 - e^{2i\beta W})}{(1 - \rho^2 e^{2i\beta W})} \quad (3)$$

where ρ is the Fresnel coefficient. The resonances can be found by calculating the poles $\tilde{\omega}$ in the complex plane of the reflection coefficient ([SI](#)). The real part of the poles corresponds to the resonant angular frequencies while the imaginary part is related to the quality factor Q of the cavity (being ratio of the stored energy to the energy dissipated per oscillation cycle). The analytical calculations of the poles give:

$$\lambda_{(q)} = \frac{2n_{eff}W}{q} \quad (4)$$

$$Q_{(q)} = -q \frac{\pi}{2 \ln|\rho|} \quad (5)$$

where q is the resonance order. For a ribbon of width $W = 2 \mu\text{m}$, three resonant wavelengths are found in the spectral range of the PL emission, 585 nm, 643 nm and 714 nm for q equal 11, 10 and 9, respectively, whose quality factors are around 11. This demonstrates that photons emitted by the ZnO NWs are trapped and constructively interfere within the ribbons, explaining the enhancement of the PL for ZnO NW gratings. Remark that we could even expect larger Q factors since the ribbons are bidimensional cavities that better trap the photons. However, the electromagnetic coupling between adjacent ribbons must be considered for ameliorating this simple picture. For that purpose, we have calculated the dispersion relation of the grating using a finite element method implemented in the software Comsol Multiphysics [REF]. We found that the best agreement between the simulated and experimental dispersion relations occurs for a reduced ribbon's width of $1.6 \mu\text{m}$, instead of $2 \mu\text{m}$ according to the used mask. Similar dispersion relations were obtained for both TE and TM polarized light and only the eigenmodes presenting Q factors larger than 10 have been plotted (Figure 12). The reduced ribbon's width introduced here can be considered as an effective width that takes into account the decrease of NW density at the periphery of the ribbons. Remark that a symmetric experimental dispersion curve could be added by scanning the PL emission for negative detection angles. We also observed that the quality factor ranges between 17 to 26 which is larger than that obtained by the simple 1D Fabry-Perot model (around 11 as mentioned before), showing the stronger localization effect allowed by 2D cavities. The electromagnetic coupling between the ribbons slightly shifts the resonant wavelengths and lifts the degeneracy of the modes at the edge of the Brillouin zone.

Commenté [ML6]: Compléter

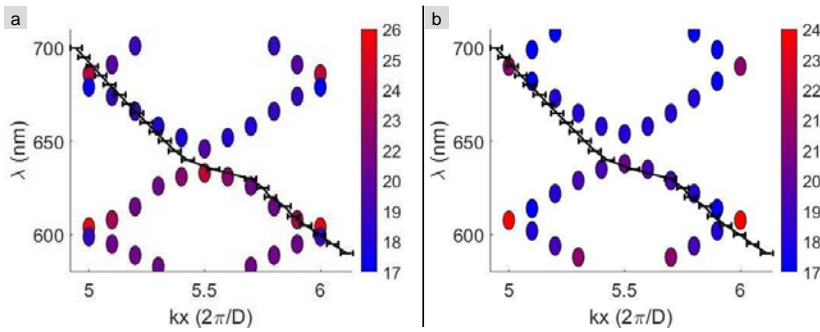


Figure 13: Colored circles: (a) and (b) are the theoretical dispersion relation for TE and TM polarizations, respectively, computed for ribbons of $1.6 \mu\text{m}$ width, 600 nm height, and $4 \mu\text{m}$ grating period. The value of the quality factor corresponds to the color of the circles. The black curve is the experimental dispersion relation.

Although the emitted photons could be radiated by several diffraction orders of the grating, we have experimentally observed that the enhanced PL emission occurs only for angles lying from 50° to 70° . The selection of the fifth and sixth diffraction orders is explained by the phase matching condition between the guided modes and the radiated plane waves^[35]. Assuming that the wavenumber of the guided modes within the periodic truncated waveguides is close to that for the infinite waveguide, the Bragg scattering condition leads:

$$k_x \approx \pm\beta \pm p2\pi/D \quad (6)$$

where p is an integer. The diffraction angles are then approximatively obtained by:

$$\sin\theta_p \approx \pm n_{eff} \pm p\lambda/D \quad (7)$$

Since $-1 \leq \sin\theta_p \leq 1$, the first diffraction order that satisfies this condition is $p=5$ explaining that the enhanced PL is collected for $5 \frac{2\pi}{D} \leq k_x \leq 6 \frac{2\pi}{D}$.

These conclusions are confirmed by the electromagnetic simulations that allow us to compute the map of electric field of the eigenmodes and their radiated power in the far-field, gathered in Figure 13. For example, for a TE polarized light, $k_x = 6 \frac{2\pi}{D}$ and the 604 nm wavelength, the electric field clearly resonates into the ZnO ribbon, and we recognize the fundamental mode of the infinite waveguide (guided within the ZnO coating) (Figure 5x). This result attests that the resonance mechanism can only be attributed to the fundamental mode since the antisymmetric one plays a negligible role because of its low Q factor. The near field map also shows a large amount of electric field outside the ribbon, highlighting the strong electromagnetic coupling with its neighbors. Lastly, the angular distribution of the far-field intensity shows that the emission is coupled out at 60° and at the symmetric direction (300°) (Figure 13b) (Figure b).

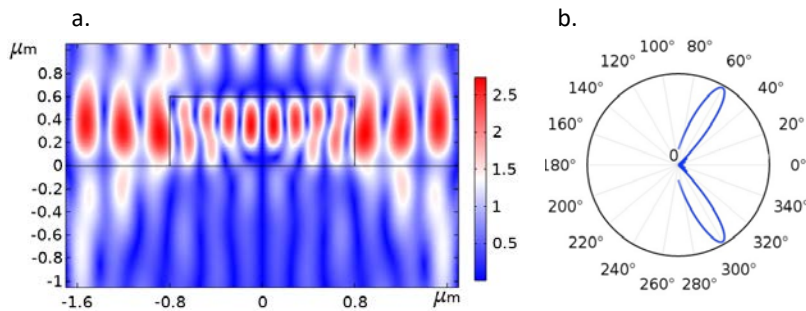


Figure 14: (a) Map of the modulus of the electric field (for TE polarization) in the near field at 604 nm for $k_x = 6 \frac{2\pi}{D}$. (b) Angular representation of the far field intensity (in a.u.) of the eigenmode.

The effective model established therefore explains that the exaltation of photoluminescence originates both from coupled cavity resonances together with a diffraction mechanism that enable the extraction of the resonant photons towards some specific angles.

Conclusion

In this work, we have presented an original way to elaborate luminescent ZnO NW-based architectures. A sol-gel derived Zn-BzAc photoresist has first been deposited by spin-coating on silicon or quartz substrate. After crystallization at 540°C , this resist serves as seed layer for the subsequent growth of ZnO NWs by hydrothermal synthesis at ambient pressure. This procedure allows the elaboration of samples with NWs fully covering the substrate (NWs coating); using a preliminary selective insolation of the photoresist, it lead to samples constituted of NW gratings. On the basis of SEM and AFM characterizations, we have firstly shown how the optimization of key experimental parameters, in particular the precursor concentration in the bath used for NW growth and the light power during the resist insolation step, enables to set up a robust protocol leading to uniform and reproducible NW linear and periodic gratings with a width / pitch of $2 \mu\text{m} / 4 \mu\text{m}$. Optimized conditions have been defined as a concentration of the zinc precursor in solution of 0.0125M and an insulating power of $25 \text{ mW}/\text{cm}^2$. Derived NW coating and grating-constituted samples have then been thoroughly characterized by standard PL and ARPL measurements. Former optical characterizations show that, under UV excitation (375 nm), both kinds of samples similarly emit light in the orange-red spectral range (around 600 nm), which is attributed to radiative transitions induced by structural

defects at the surface of ZnO NWs. In contrast, ARPL intensity measurements and mapping demonstrate that light emission is considerably influenced by the presence of NW gratings, showing that these ones enable to strongly enhance the extraction of light emitted by the ZnO NWs and trapped as guided modes into the NW layer in the case of a full covered sample. This enhancement proceeds in a selective range of emission angles, between 50 and 70°. More specifically, for angles lying in the 58-62° range, the grating structure makes it possible to exalt specific wavelengths in the red spectral range (up to 700-750 nm) that are largely exceeding the emission wavelength intrinsically due to the NWs. Electromagnetic simulations have then been performed to explain these features. For that purpose, an effective model has been developed where the complex random spatial distribution of NWs is simulated by homogeneous solid ribbons. The good agreement between the theoretical dispersion relation derived from this model and the experimental one enables to validate the suggested model. This latter finally allows proposing a phenomenological and quantitative description showing the role of microcavities played by the ZnO NW gratings. In this description, the PL emission is boosted thanks to coupled cavity resonance phenomena together with a diffraction mechanism, which i/ enables the extraction of the resonant photons towards some specific angles and at given wavelengths, and ii/ supports experimental results arising from PL measurements. These specific features could be put to good use in applications where specific spatial extraction is useful such as anti-counterfeiting marking. Other gratings configurations have to be studied to better apprehend the influence of gratings parameters on the aforementioned phenomena.

Funding:

This work was supported by the French “Agence Nationale de la Recherche” for its financial support in the frame of the ANR SMARTLEDs project (ANR-19-CE08-0001).

References

- [1] M. Liu, P. Jin, Z. Xu, D. A. H. Hanaor, Y. Gan, C. Chen, *Theoretical and Applied Mechanics Letters* **2016**, *6*, 195.
- [2] S. Alagha, A. Shik, H. E. Ruda, I. Saveliev, K. L. Kavanagh, S. P. Watkins, *Journal of Applied Physics* **2017**, *121*, 174301.
- [3] H. Zhu, in *Nanowires - New Insights* (Ed.: K. Maaz), InTech, **2017**.
- [4] P. Yu, J. Wu, S. Liu, J. Xiong, C. Jagadish, Z. M. Wang, *Nano Today* **2016**, *11*, 704.
- [5] K. Chen, D. D. Thang, S. Ishii, R. P. Sugavaneshwa, T. Nagao, *Opt. Mater. Express* **2015**, *5*, 353.
- [6] N. Zhou, B. C. Hu, Q. Y. Zhang, C. Y. Ma, S. Z. Hao, *AIP Advances* **2019**, *9*, 045004.
- [7] H. Dittlacher, A. Hohenau, D. Wagner, U. Kreibitz, M. Rogers, F. Hofer, F. R. Aussenegg, J. R. Krenn, *Phys. Rev. Lett.* **2005**, *95*, 257403.
- [8] S.-Y. Hsu, M.-C. Lee, K.-L. Lee, P.-K. Wei, *Appl. Phys. Lett.* **2008**, *92*, 013303.
- [9] M. Djavid, Z. Mi, *Appl. Phys. Lett.* **2016**, *108*, 051102.
- [10] H. Jeong, D. J. Park, H. S. Lee, Y. H. Ko, J. S. Yu, S.-B. Choi, D.-S. Lee, E.-K. Suh, M. S. Jeong, *Nanoscale* **2014**, *6*, 4371.
- [11] L. Huang, F. Zhang, D. Yuan, B. Liu, C. Cheng, *Physica E: Low-dimensional Systems and Nanostructures* **2022**, *142*, 115326.
- [12] N. Ganesh, W. Zhang, P. C. Mathias, E. Chow, J. A. N. T. Soares, V. Malyarchuk, A. D. Smith, B. T. Cunningham, *Nature Nanotech* **2007**, *2*, 515.
- [13] K. McGroddy, A. David, E. Matioli, M. Iza, S. Nakamura, S. DenBaars, J. S. Speck, C. Weisbuch, E. L. Hu, *Appl. Phys. Lett.* **2008**, *93*, 103502.
- [14] J. J. Wierer, A. David, M. M. Megens, *Nature Photon* **2009**, *3*, 163.
- [15] J. H. Lin, C.-Y. Tseng, C.-T. Lee, H.-C. Kan, C. C. Hsu, *Opt. Express* **2013**, *21*, 24318.
- [16] H. Park, K.-J. Byeon, K.-Y. Yang, J.-Y. Cho, H. Lee, *Nanotechnology* **2010**, *21*, 355304.
- [17] C. Zhang, X. Huang, H. Liu, S. J. Chua, C. A. Ross, *Nanotechnology* **2016**, *27*, 485604.
- [18] M. Khaywah, A. Potdevin, F. Réveret, R. Mahiou, Y. Ouerdane, A. Désert, S. Parola, G. Chadeyron, E. Centeno, R. Smaali, A. Moreau, *J. Phys. Chem. C* **2021**, *125*, 7780.
- [19] K.-G. Lee, K.-Y. Choi, S.-H. Song, *Current Applied Physics* **2014**, *14*, 1771.
- [20] G. Lozano, S. R. Rodriguez, M. A. Verschuuren, J. Gómez Rivas, *Light Sci Appl* **2016**, *5*, e16080.
- [21] B. A. Albiss, M.-A. AL-Akhras, I. Obaidat, *International Journal of Environmental Analytical Chemistry* **2015**, *95*, 339.
- [22] A. Singh, S. Singh, *Bull Mater Sci* **2018**, *41*, 94.
- [23] H. H. Tran, R. B. Venkatesh, Y. Kim, D. Lee, D. Riassetto, *Nanoscale* **2019**, *11*, 22099.
- [24] C. Cheng, M. Lei, L. Feng, T. L. Wong, K. M. Ho, K. K. Fung, M. M. T. Loy, D. Yu, N. Wang, *ACS Nano* **2009**, *3*, 53.
- [25] P. Obreja, D. Cristea, A. Dinescu, C. Romanitan, *Applied Surface Science* **2019**, *463*, 1117.
- [26] M. Maddah, C. P. Unsworth, N. O. V. Plank, *Mater. Res. Express* **2018**, *6*, 015905.

- [27] G. P. Papageorgiou, A. G. Karydas, G. Papageorgiou, V. Kantarelou, E. Makarona, *Micro and Nano Engineering* **2020**, *8*, 100063.
- [28] H.-H. Park, X. Zhang, K. W. Lee, K. H. Kim, S. H. Jung, D. S. Park, Y. S. Choi, H.-B. Shin, H. K. Sung, K. H. Park, H. K. Kang, H.-H. Park, C. K. Ko, *CrystEngComm* **2013**, *15*, 3463.
- [29] T. Demes, C. Ternon, D. Riassetto, V. Stambouli, M. Langlet, *J Mater Sci* **2016**, *51*, 10652.
- [30] T. Kawahara, T. Ishida, H. Tada, N. Tohge, S. Ito, *JOURNAL OF MATERIALS SCIENCE LETTERS* **2002**, *21*, 3.
- [31] T. Kawahara, T. Ishida, H. Tada, N. Noma, N. Tohge, S. Ito, *JOURNAL OF MATERIALS SCIENCE LETTERS* **2003**, *38*, 5.
- [32] N. Amara, A. Martin, A. Potdevin, D. Riassetto, M. Messaoud, F. Réveret, G. Chadeyron, J. Bouaziz, M. Langlet, *Journal of Alloys and Compounds* **2020**, *842*, 155708.
- [33] V. A. Markel, *J. Opt. Soc. Am. A* **2016**, *33*, 1244.
- [34] B. E. A. Saleh, M. C. Teich, *Fundamentals of Photonics, 2nd Edition*, **2007**.
- [35] D. G. Hall, in *Progress in Optics*, Elsevier, **1991**, pp. 1–63.